Thesis for the degree of Licentiate of Engineering

Modelling optical properties of morphologically complex soot aerosols

Franz Kanngießer

Department of Space, Earth and Environment
CHALMERS UNIVERSITY OF TECHNOLOGY
Göteborg, Sweden 2019

Modelling optical properties of morphologically complex soot aerosols
Franz Kanngiesser

Department of Space, Earth and Environment
Chalmers University of Technology
SE–412 96 Göteborg, Sweden
Telephone + 46 (0) 31 – 772 1000

Example of a modelled soot aggregate: one time as bare (uncoated) aggregate and two times as thickly coated aggregate. The two coated aggregates illustrate the two model realisations discussed in Paper A.

Typeset by the author using LaTeX.

Printed by Chalmers Digitaltryck
Göteborg, Sweden 2019

Modelling optical properties of morphologically complex soot aerosols
Franz Kanngiesser
Department of Space, Earth and Environment
Chalmers University of Technology

Abstract

Soot containing aerosol has both adverse impacts on the Earth's climate and on human health. Monitoring soot sources, transport pathways and sinks on global scale requires satellite-borne remote sensing techniques.

A detailed understanding of the soot particle's optical properties is important to improve the interpretation of remote sensing data as well as the use of lidar remote sensing data in chemical transport modelling. The calculations of the optical properties were carried out using the discrete dipole approximation (DDA). Aim of this thesis is to identify key morphological features, which affect the depolarisation ratio.

As soot particles age in the atmosphere, condensation of other compounds from the gas phase onto the particles results in soot aggregates coated by liquid-phase material. Initially, the soot particles are coated by a thin film (i.e., the coating follows the shape of the aggregate). As more liquid phase material is added, the coating becomes increasingly spherical. It is found that this transition from film coating to radial growth of spherical shells is an important process affecting the linear depolarisation ratio. If this transition occurs first at relatively high amounts of coating, then the depolarisation ratio tends to be high. Conversely, if the coating becomes already spherical at low amounts of coating material, then the depolarisation ratio of the coated soot particles is much lower.

The linear depolarisation ratio of thickly coated aggregates was found to be sensitive to changes in the complex refractive index of the coating material, which represents changes in the chemical composition. These differences in the optical properties, even after averaging over a particle size distribution, are large enough to clearly distinguish the coating materials.

Keywords: black carbon, aerosol, depolarisation, scattering, lidar, remote sensing.

Acknowledgments

I am very grateful for the opportunity to begin my PhD studies at Chalmers University of Technology, which itself was possible thanks to funding from the Swedish Research Council.
First and foremost I would like to thank Michael for advice and guidance. Navigating a different part of university life can have its very own challenges on top of a research project's challenges. Therefore, I would like to thank my colleagues for the advice and feedback I received. And I would also like to thank all the regular and not so regular attendants of the coffee breaks on floor 4ö for interesting discussions, new insights and (during the recent months) opportunities to practice my Swedish.

Franz Kanngießer
Göteborg, November 2019

List of Publications

This thesis is based on the following appended papers:

Paper A. Franz Kanngießer and Michael Kahnert. *Calculation of optical properties of light-absorbing carbon with weakly absorbing coating: A model with tunable transition from film-coating to spherical-shell coating.* J. Quant. Spectrosc. Radiat. Transfer, 2018.

Paper B. Franz Kanngießer and Michael Kahnert. *Coating material-dependent differences in modelled lidar-measurable quantities for heavily coated soot particles.* Submitted to Opt. Express.

Contents

Part I

Introductory chapters

Chapter 1

Introduction

According to the latest assessment report of Working Group 1 of the Intergovernmental Panel on Climate Change (IPCC), which covers the underlying physical science basis on climate change, aerosol particles are affecting the radiative forcing in various ways. The understanding of various aerosol related effects on climate has increased throughout the past IPCC reports. Compared to previous reports the confidence level regarding changes in radiative forcing due to aerosol radiation interactions has increased to "high". However, other aspects, such as changes in the albedo due to the deposition of black carbon aerosol on snow and ice, aerosol-cloud interactions are considered to have a "low" confidence level, or the total aerosol effect has a "medium" confidence level (Myhre et al. 2013).

Aerosol particles not only play a role in various elements of the Earth's climate system, they can have various adverse impacts on human health (Pöschl 2005). Among those impacts on human health are shortened life expectancies and increases in pulmonary, cardiovascular and allergic diseases.

Regarding both the impacts on the anthropogenic radiative forcing and negative impacts on human health, aerosol particles containing soot (or black carbon, as it is sometimes called) play an import role. Black carbon is besides carbon dioxide and methane one of the main drivers of anthropogenic climate change (Bond et al. 2013; Myhre et al. 2013). Black and organic carbon are also associated with premature deaths and pulmonary diseases (Anenberg et al. 2011; Anenberg et al. 2012).

Both the climate and the human health impacts motivate studies of soot emission sources, transport pathways and sinks. This monitoring requires the use of remote sensing techniques. The interpretation of remote sensing measurements and the use of remote sensing data in chemical transport modelling in turn requires a thorough understanding of the optical properties of soot particles.

This thesis aims at improving the understanding of soot optical properties by proposing a tunable model for coated soot particles. The potential use of the model in remote sensing applications is investigated.

Chapter 2

Earth's atmosphere

2.1 Atmospheric composition and structure

The Earth's atmosphere consists of 78% nitrogen (N_2), of 21% oxygen (O_2), and of 0.7% argon (Ar) and various trace gases. While these trace gases have a low concentration they are important for the Earth's radiative energy budget (green house gases such as carbon dioxide and methane) and for air quality. The dry atmosphere can be considered well mixed up to an altitude of about 100 km. This means that the atmosphere's components can be considered having a constant mixing ratio.

Based on the change of the temperature variation with altitude the atmosphere can be divided into further layers. Starting from the bottom these layers are the troposphere, stratosphere, mesosphere, thermosphere and exosphere. The layers are divided by layers of constant temperature. The boundary between tropos- and stratosphere is called tropopause, the boundary between stratos- and mesophere is called stratopause and consequently the boundary between mesosphere and thermosphere is called mesopause. The exosphere is the outermost region of the atmosphere above 500 km height. Here gas molecules with enough kinetic energy can escape into space (Wells 2011).

The temperature increase in the stratosphere is caused by the ozone layer at 20-30 km height. Since ozone is highly reactive it does not remain in the atmosphere long enough to become well-mixed (Seinfeld and Pandis 2016; Wells 2011). The increase in atmospheric temperature in the stratosphere is caused by ozone absorbing radiation and the photodissociation of ozone (Wells 2011).

The pressure $p(z)$ at height z can be calculated by[1]:

$$p(z) = p_0 \exp\left(\frac{-zg_0}{R\bar{T}}\right) \tag{2.1}$$

Here p_0 denotes the mean pressure at sea level with $p_0 = 1013.25\,\mathrm{hPa}$. g_0 =9.806 65 $\mathrm{m\,s^{-2}}$ is the global average of the gravitational acceleration at sea level. R is the specific gas constant for dry air (R =287 $\mathrm{J\,kg^{-1}\,K^{-1}}$) and $\bar{T}$ is the mean temperature of the

[1]Strictly speaking the equation is valid for the geopotential height Z which is numerically almost identical to the geometric height z. A more detailed account on the geopotential height is provided by Holton (2004).

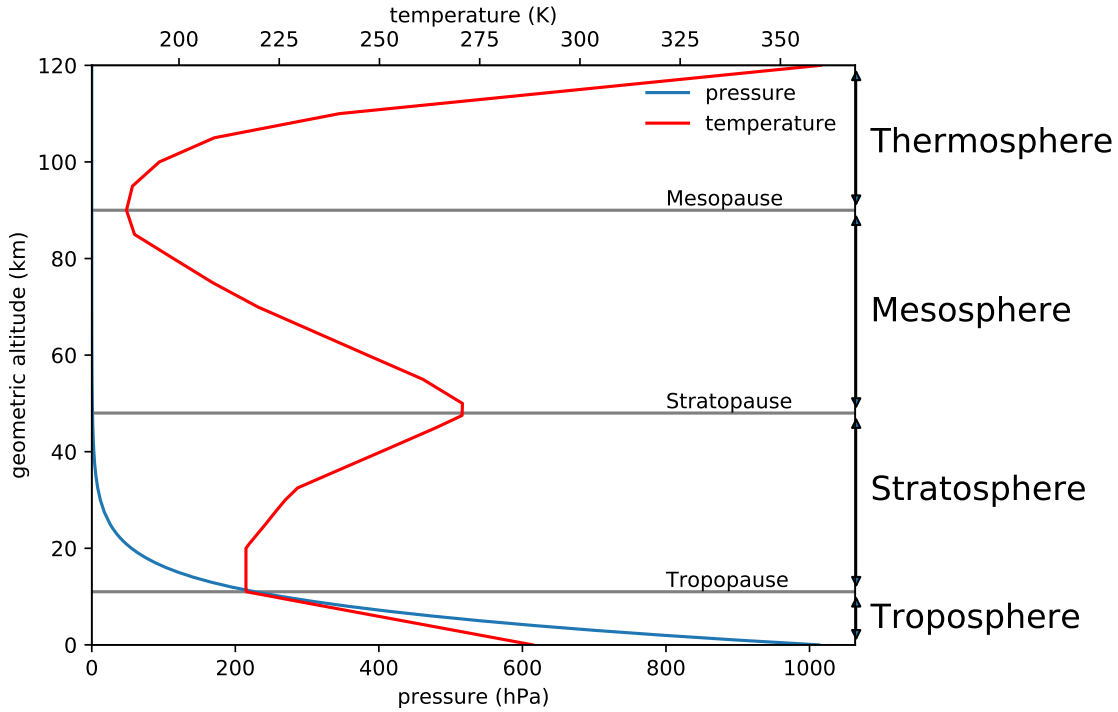

Figure 2.1: Temperature and pressure profile of the U.S. Standard Atmosphere (1976)

layer between sea level and z in Kelvin. In an isothermal atmosphere the pressure decreases exponentially with height.

A number of applications, such as aircraft and rocket design, aircraft performance tests (U.S. Commitee on Extension of the Standard Atmosphere 1976) or in certain cases even remote sensing applications (see Section 3.2), require standardised atmospheric profiles, which show typical values of atmospheric propeties for a specific height. These are referred to as standard atmospheres, a prominent example is the U.S. Standard Atmosphere of 1976 (U.S. Commitee on Extension of the Standard Atmosphere 1976). Figure 2.1 shows the temperature (red line) and the pressure (blue line) profile according to this standard atmosphere.

Water vapour is a highly variable component of the atmosphere and as such not well-mixed. The mass fraction of water vapour ranges from 0 to 4.3%. The amount of water vapour in the atmosphere depends on the air temperature. This temperature-dependence prevents water vapour from becoming well-mixed (Wells 2011). As the tropospheric temperature decreases with height so does the water vapour content. For example, in the US Standard Atmosphere (1976) about 90% of the water vapour mass are in the lowest 5 km of the atmosphere (U.S. Commitee on Extension of the Standard Atmosphere 1976).

The troposphere can be further divided into the atmospheric boundary layer and the free troposphere. The boundary layer is the layer reaching from the surface to an altitude of usually 1 to 2 km. The boundary layer is usually defined as the part of the troposphere directly affected by the surface, for example by friction. The free troposphere, which is above the boundary layer, is not directly affected by the

surface (Stull 1988).

The transition from boundary layer to the free troposphere is often characterised by a temperature inversion (i.e. the the temperature is constant or increasing with increasing altitude instead of decreasing) (Stull 1988). Temperature inversions, especially when sufficiently strong, suppress upward motion of air (Holton 2004; Stull 1988). This temperature inversion caps upward motion, and strato-cumulus clouds form at the top of the boundary layer. These clouds can enhance the temperature inversion and thereby block upward motion more effectively. An alternative view of the boundary layer describes the boundary layer not according to the influence of the surface, but according to the impacts associated with this layer of stratocumulus clouds (Wood 2012).

By the temperature inversion at the top of the boundary layer suppressing upward motion pollutants and water vapour may become trapped inside the boundary layer. The conditions in the boundary layer can affect the formation of natural atmospheric aerosol particles (Boucher 2015).

2.2 Atmospheric aerosol

Liquid or solid particles suspended in air are referred to as atmospheric aerosol particles. By convention in atmospheric sciences hydrometeors (cloud droplets, cloud ice and precipitation) are usually not considered aerosol particles. As the definition of aerosol particles is rather broad, there are various ways to classify aerosol particles.

Aerosols can be divided into two types based on their formation: primary and secondary aerosol particles. Primary aerosol particles get emitted into the atmosphere as particle. Examples include soot from incomplete combustion processes or aerosol particles originating from wind friction on an oceanic or a terrestrial surface. Secondary aerosol particles are not directly emitted into the atmosphere but form by condensation of gas-phase species. These gas-phase species are called aerosol precursors (Boucher 2015).

Aerosol particles are found in the two lower layers of the atmosphere: the troposphere and the stratosphere. Aerosol particles and their respective precursors are usually directly emitted into the troposphere. Tropospheric air masses are almost exclusively transported into the stratosphere in the tropics. A large portion of stratospheric aerosol particles can be traced back to volcanic eruptions, but deep convection and convection caused by strong wild fires can inject black carbon and biomass burning aerosol into the stratosphere (Boucher 2015).

Aerosol particles remain a few days up until two weeks in the troposphere until they are deposited. Aerosol particles are removed from the atmosphere by being washed out (wet deposition), by being carried to the surface by turbulent fluxes (dry deposition), and by being deposited by gravitation (sedimentation). In the stratosphere however, aerosol particles usually remain for six months up to two years (Boucher 2015).

In addition to the classification based on the formation or the occurrence in an atmospheric layer aerosol particles can be classified according to their environment, such as urban aerosol particles.

2.2.1 Aerosol sources

Another way of classifying aerosol particles is according to their sources: marine aerosol, desert or mineral dust aerosol, volcanic aerosol, biogenic aerosol and aerosol from biomass and fossil fuel burning are common types (Boucher 2015). Marine aerosols or sea spray aerosol originate from sea water ejected from the ocean. Although it mainly consists of sea salt it can contain biogenic material as well as other impurities. The typical size range is between 100 nm and tens of micrometers. The annual emission flux of sea spray aerosol is between 1000 - 6000 Tg (1 Tg = 10^{12} g = 1,000,000 tons).

Desert dust or mineral dust aerosol is caused by wind friction over continental surfaces mostly in desertic, arid and semi-arid regions. Desert dust particles span a similar size range as marine aerosol particles. 1000 - 3000 Tg of mineral dust aerosol particles are estimated to be emitted annually.

Volcanoes emit volcanic ash, fragments of pulverised rock, and minerals. Volcanic ash particles tend to cover a size range from a few micrometers to millimetres. Additionally, sulphur-containing gases are emitted, which can form secondary aerosol particles or condense onto other particles. Tropospheric volcanic aerosol has a short residence time in the troposphere. However, strong volcanic eruptions can eject volcanic material into the stratosphere where residence times are longer. Thus the aerosol can have impacts on the climate.

Biogenic aerosols consist of pollen, spores, bacteria, viruses and debris of plants and insects. The total annual emission of primary biogenic particles is on the order of 1000 Tg. This includes the mass of emitted bacteria estimated to be in between 40 - 1800 Gg, and the mass of emitted spores estimated to be 30 Tg. Plant and insect debris are often larger than 100 µm, and thus are usually sedimentated quickly. Pollen, spores and large bacteria have a particle size between 1 and 100 µm while viruses and small bacteria are smaller than 1 µm. Ecosystems are an important source of aerosol precursors which then can form secondary biogenic aerosol.

Both biomass burning aerosols and aerosols from fossil fuel combustion contain black and organic carbon. Organic carbon contains a relatively high number of hydrogen and oxygen atoms while black carbon has a higher number of carbon atoms. The aerosol particles are usually smaller than a micrometer. 70 - 125 Tg of biomass burning aerosol are estimated to be emitted annually and 26-40 Tg from fossil fuel burning. Burning of biomass and fossil fuel leads to the emission of precursor gases.

Most of these aerosol sources are located at the Earth's surface. As previously explained upward motion of air is suppressed by temperature inversions. This accounts for the limited entrainment of aerosol particles into the stratosphere, but also causes most aerosol particles to remain in the boundary layer, the lowermost part of the troposphere (Boucher 2015).

2.2.2 Aerosol effects

As there are various different types of aerosol particles the impacts of aerosol particles are equally diverse.

Aerosol particles have a number of different impacts on the climate system: aerosol particles scatter and absorb solar radiation directly. The absorption of solar radiation by aerosol particles changes the temperature profile, which impacts cloud formation by affecting relative humidity and atmospheric stability. Cloud formation processes are additionally impacted by aerosol particle acting as cloud condensation nucleii. An increase in cloud condensation nucleii results in an increase of cloud droplet concentration. An increase in cloud condensation nucleii with otherwise unchanged conditions results in smaller cloud droplets, which cause clouds to have a higher reflectivity. Aersosol particles also act as ice nucleii and thus can initiate glaciation in liquid water and mixed phase clouds. Absorbing aerosol particles deposited on snow and ice surfaces reduces the surface albedo. And last aerosol particles interact with vegetation by changing the incoming solar radiation and by acting as nutrients (Boucher 2015; Seinfeld and Pandis 2016).

As mentioned briefly in Chapter 1 not all effects of aerosol particles on the climate are well understood. There are different metrics to examine effects on the Earth's climate. The metric used by the IPCC is the radiative forcing (RF). It describes the net change of the energy balance caused by some pertubation and is defined as the change in downward radiative flux at the tropopause. The changes in radiative forcing, caused by the direct interaction of radiation and aerosol particles are very well understood. However, the effects caused by aerosol cloud interactions and the changes in the surface albedo, caused by aborbing aerosol particles deposited on ice and snow, are less understood. In the terminology of the IPCC the confidence in radiative forcing changes due to these effects is low. The total aerosol effect on changes in radiative forcing has a medium level of confidence (Myhre et al. 2013). Aerosol particles in general have a cooling effect (i.e., a negative radiative forcing), except for strongly absorbing aerosol.

Atmospheric aerosol particles can be linked to different adverse impacts on human health, including cardiovascular, respiratory, and allergic diseases as well as increased mortality (Pöschl 2005).

Increasing the number of aerosol particles decreases atmospheric visibility (Seinfeld and Pandis 2016). Atmospheric visibility refers to the range at which a large black object can be seen against the horizon. This range is affected by absorption and scattering by aerosol particles and molecules in the atmosphere. Changes in colouration and/or light intensity of the sky or nearby objects allow for subjective judgements regarding the visibility in absence of far objects.

Aerosol particles can even impact air traffic: Due to its highly abrasive nature volcanic ash particles can damage aircraft wind shields, engines and electronics (Casadevall 1994).

Both mineral dust aerosol particles and soot aerosol particles dominate the ice nucleii which initiate immersion freezing in supercooled liquid droplets for a temperature above $-15\,°C$ (Hoose et al. 2010; Murray et al. 2012). For lower temperatures biogenic aerosol particles dominate the ice nucleii (Murray et al. 2012).

As previously mentioned, biomass burning aerosol and aerosol from fossil fuel combustion contain large amount of highly absorbing carbonaceous material, often referred to as soot or black carbon. As soot containing aerosol is highly absorbing,

it is one of the largest drivers for anthropogenic climate change (Bond et al. 2013). 40% of the reduction in visibility in urban areas can be attributed to carbonaceous particles (Seinfeld and Pandis 2016). In addition to the adverse impacts of soot aerosol on the Earth's climate and on air quality black carbon aerosol belongs to the various aerosol types that have a pronounced negative impact on human health, such as increased mortality from cardiopulmonary diseases and lung cancer (Anenberg et al. 2011; Anenberg et al. 2012). As a consequence, there are co-benefits for climate and air quality from soot emission reductions (Anenberg et al. 2012), unlike, e.g. sulphate emissions, which have a cooling effect on the Earth's climate (Myhre et al. 2013), but a negative impact on air quality (e.g., Anenberg et al. 2011).

Chapter 3

Remote sensing of aerosol particles

Monitoring of atmospheric aerosol particles on a global scale using satellite systems or unperturbed by in situ sampling methods requires the use of remote sensing techniques. These techniques are usually divided into passive and active techniques. Both types are used for obtaining aerosol properties. The stronger emphasis here will, however, be on active remote sensing techniques. Section 3.1 is largely based on (Boucher 2015), while Sections 3.2 and 3.3 are based on (Ansmann and Müller 2005), if not otherwise indicated.

3.1 Passive remote sensing

Passive remote sensing describes measurement of electromagnetic waves emitted or scattered from the object of interest. A common use of passive aerosol remote sensing is the determination of the aerosol optical thickness by measuring the received radiation. The optical depth is the sum of the aerosol optical thickness and the molecular optical thickness. The extinction by molecules can be estimated from the surface pressure, if the molecular absorption is considered negligible. The measured solar irradiance F at wavelength λ is related to the solar irradiance at the top of the atmosphere F_0 and the optical thickness τ by:

$$F_\lambda = F_{0,\lambda} \exp\left[-\tau(\lambda)\right] \tag{3.1}$$

The optical thickness for aerosol particles $\tau_a(\lambda)$ with homogeneous properties in a layer with the geometrical thickness Δz can be calculated from the extinction efficiency Q_{ext}, which relates the light extinction by a particle to its geometric cross section (see Section 4.1), and the aerosol size distribution $n(r)$:

$$\tau_a(\lambda) = \Delta z \int \pi r^2 Q_{ext}(r, \lambda) n(r) dr \tag{3.2}$$

Measurements of the optical thickness at multiple wavelengths allows us to obtain the aerosol size distribution $n(r)$. However this method is limited to radii smaller than 4 µm (Boucher 2015). The NASA-coordinated AERONET (Aerosol Robotic Network) uses sun photometers, which measure both direct and diffuse radiation. The combination of direct and diffuse radiation at multiple wavelengths allows,

additionally, the retrieval of the single scattering albedo for optical thicknesses larger than 0.4 (Boucher 2015).

Light emitted by the sun is unpolarised, but reflection by surfaces and scattering by molecules and aerosol particles partly polarise light. Measuring polarised reflectance from space allows for an easier correction of surface contributions in the signal than measuring non-polarised reflectance from space. Information on the amount and properties of aerosol particles, including a differentiation between spherical and non-spherical particles, can be retrieved from space-borne measurements of the polarised reflectance. One instrument capable of such measurements is the POLDER (Polarization and Directionality of the Earth's Reflectance) spectroradiometer.

Another form of passive remote sensing is the measurement of the brightness temperature in the infrared spectral region. The brightness temperature corresponds to the temperature that a black body emitting the same radiance would have. Satellites such as AIRS (Advanced Infrared Radiation Sounder) or IASI (Infrared Atmospheric Sounder Interferometer) use radiometer measurements to retrieve humidity and temperature. By minimising a cost function the size distribution and the altitude of an aerosol layer can be obtained.

3.2 Active remote sensing

In active remote sensing the scattered or reflected electro-magnetic waves which were previously emitted by an instrument are measured. For remote sensing of aerosol properties lidar (light detection and ranging) instruments are used.

For the simplest form of the lidar equation valid for elastic backscattering lidars the reader is referred to Ansmann and Müller (2005). For extinction profiling mainly two types of lidar instruments are used: Raman lidar instruments and high spectral resolution lidar (HSRL) instruments. A Raman lidar measures elastically backscattered light from air molecules and aerosol particles and inelastically backscattered light by nitrogen or oxygen molecules, so called Raman scattering. The HSRL uses differences in the spectral distribution of elastically backscattered light, caused by Doppler shifts due to thermal motion.

The lidar equation relates the transmitted laser pulse energy E_0 to the molecular backscatter signal P at range R by:

$$P(R, \lambda_{Ra}) = \frac{E_0 \eta_{\lambda_{Ra}}}{R^2} O(R, \lambda_{Ra}) \beta_{Ra}(R, \lambda_0) \cdot \exp\left(- \int_0^R [\alpha(r, \lambda_0) + \alpha(r, \lambda_{Ra})] \mathrm{d}r \right) \tag{3.3}$$

In the Raman case β_{Ra} is the Raman backscattering coefficient and in Rayleigh case it is the Rayleigh backscattering coefficient. In case of rotational Raman and Rayleigh backscattering $\lambda_{Ra} = \lambda_0$. For vibration-rotational Raman scattering the wavelength shift has to be taken into account. The extinction coefficient on the way from the instrument to the backscatter region is $\alpha(R, \lambda_0)$ and $\alpha(R, \lambda_{Ra})$ is the extinction coefficient of the way from the backscatter region to the instrument. The optical and detection efficiencies of the lidar system are described by η. $O(R, \lambda_{Ra})$ is

the overlap term describing the overlap between the emitted and the detected signal. For large ranges R it becomes $O(R, \lambda_{Ra}) \equiv 1$.

The molecular backscattering coefficient $\beta_{Ra}(R, \lambda_0)$ can be calculated from the number density of molecules $N_{Ra}(R)$ and the molecular differential scattering cross section at the laser wavelength λ_0 and in backscattering direction. In case of Raman scattering $N_{Ra}(R)$ is the nitrogen or oxygen number density and in the Rayleigh case it is the number density of air molecules. The number density of molecules can be obtained either by measurements from radiosondes or from temperature and pressure profiles taken from a standard atmosphere (see Chapter 2).

With the help of the lidar equation it is possible to obtain expressions for the height profiles of the aerosol extinction coefficient α^{aer} and the aerosol backscattering coefficient β^{aer} (a derivation of the expressions was provided by Ansmann and Müller (2005)). For determining β^{aer} additional measurements of the total backscattered and molecular backscattered signal are required.

The height profile of the extinction-to-backscatter ratio (sometimes referred to as lidar ratio) than can be calculated as:

$$S_p(R, \lambda_0) = LR(R, \lambda_0) = \frac{\alpha^{aer}(R, \lambda_0)}{\beta^{aer}(R, \lambda_0)} \tag{3.4}$$

In addition to the measurement of the extinction and backscatter coefficients some lidar instruments are capable of measuring the linear depolarisation ratio. The measurement of the linear depolarisation ratio at one wavelength requires two receiver channels and careful calibration (Freudenthaler 2016). The linear depolarisation ratio indicates changes in the state of polarisation state of the emitted and received radiation. If the laser pulses emitted by a lidar interact with particles, the polarised laser light can become less polarised (depolarised). The depolarisation is quantified by the linear depolarisation ratio. For homogenous spheres the polarisation state in the backscatter direction is unchanged, thus the linear depolarisation ratio is zero. By measuring the parallel- ($P_\parallel$) and cross-polarised ($P_\perp$) backscattered power or the respective backscattering coefficients the volume depolarisation ratio can be obtained (Freudenthaler et al. 2009):

$$\delta^v = \frac{P_\perp}{P_\parallel} = \frac{\beta_\perp}{\beta_\parallel} \tag{3.5}$$

Both the depolarisation by air molecules and the depolarisation by particles contribute to the volume depolarisation ratio.

The molecular depolarisation ratio can usually obtained with high accuracy using:

$$\delta^{mol} = \frac{\beta_\perp^{mol}}{\beta_\parallel^{mol}} \tag{3.6}$$

In case the cross- and parallel-polarised particle backscatter coefficient are available the particle depolarisation ratio can be calculated analogous to Eq. (3.5). If such measurements are not available the particle depolarisation ratio can be calculated from the volume and the molecular depolarisation ratio (Freudenthaler et al. 2009):

$$\delta^{aer} = \frac{\beta_\perp^{aer}}{\beta_\parallel^{aer}} = \frac{(1+\delta^{mol})\delta^v \mathbf{R} - (1+\delta^v)\delta^{mol}}{(1+\delta^{mol})\mathbf{R} - (1+\delta^v)} \tag{3.7}$$

The backscatter ratio **R** is defined as:

$$\mathbf{R} = \frac{\beta^{mol} + \beta^{aer}}{\beta^{mol}} \tag{3.8}$$

The shape sensitivity of the linear depolarisation ratio is often used to discern between non-spherical cloud ice ($\delta^{aer} > 0$) and spherical, liquid cloud droplets ($\delta^{aer} = 0$) and the distinguish between dry (larger values of δ^{aer}) and wet aerosol particles ($\delta^{aer} \approx 0$) (Freudenthaler et al. 2009).

The linear depolarisation ratio can not only be used to obtain information on the cloud phase and whether aerosol particles are dry or wet, but in combination with measurements of the extinction and backscattering coefficients, it is possible to gain some insights in the microphysical properties of aerosol particles.

3.3 Retrieval of microphysical properties

With the help of the measured optical properties it is possible to retrieve physical properties of aerosol particles (Ansmann and Müller 2005).

A common approach for microphysical retrievals lies in the combination of passive sun photometer measurements and lidar measurements. From sun photometer measurements (see Section 3.1) the aerosol particle size distribution can be determined. The combination then allows for a rough estimate of the complex refractive index. The combination of two different instruments adds challenges and potential for introducing uncertainties. The main drawback is the requirement of two different instruments at the same location at the same time. An important source of errors in this retrieval type is that in most cases the sun photometer and the lidar instrument do not point into the same direction, so the measurements do not constrain the exact same volume filled with aerosol particles.

For another method Mie calculations can be used to simulate the optical properties measured by multiwavelength lidar. The shape of the particle size distribution and the complex refractive index are assumed a priori. The uncertainty due to these a priori assumptions restricts the method to specific cases: Retrievals of stratospheric aerosol particles were successful, but for tropospheric aerosol particles only a crude classification according to the aerosol type was achieved.

The third approach for microphysical aerosol retrievals is based on the combination of mathematical methods and multiwavelength lidar observations. For this approach mostly Raman lidars are used. Especially the spectral information of changes in backscatter and extinction and their connection to the particle size are used. Here the amount of a priori information introduced can be reduced compared to the second approach.

The standard approach to retrieve microphysical properties with the help of the combination of multi-wavelength lidar observations and mathematical methods (third approach) is called regularisation with constraints. The optical data is linked to physical properties by Fredholm integral equations of the first kind.

$$g_p = \int_{r_{min}}^{r_{max}} K_p(r, m) v(r) \mathrm{d}r + \epsilon_p^{exp} \tag{3.9}$$

The subscript p summarises kind (e.g. backscatter coefficient or extinction coefficient) and number (i.e. wavelength) of optical data. g_p denotes optical data at a specific range R, however the range dependence is not indicated in Eq. (3.9) for the sake of clarity. The data have an error ϵ. $v(r)$ denotes the particle volume concentration in the radius interval dr The kernel efficiencies of the optical data are described by K_p. They depend on the particle radius r and the complex refractive index m. The calculation of the kernel functions depend implicitly on the assumed particle shape. For spherical particles the optical efficiencies are used in this calculation. The lower integration limit is defined by the size at which particles are no longer optically detectable. For wavelengths larger than 355 nm this r_{min} is typically ~ 50 nm. The upper integration limit is determined by the size at which particles usually do not contribute to the signal any more owing to their low number density. In case of tropospheric particles r_{max} is usually below 10 μm

The numerical solution of these integral equations leads to an ill-posed problem. This problem is characterised by the incompleteness of the available information (caused by the limited number of measurements), the non-uniqueness of the solutions (owning to the complexity of the the aerosol sample) and the non-continuous dependence of the solutions (related to the large range of values of matrix elements in the matrix formulation of Eq. (3.9)) on the input data. The non-uniqueness of the solution is caused by the large variability of atmospheric aerosol particles (see Section 2.2). Different combinations of particle shape, size, number concentration and complex refractive index can result in optical properties which are indistinguishable within the margin of measurement uncertainty.

To provide a numerical solution Eq. (3.9) is written as a matrix equation. To avoid error amplification and the solution becoming non-unique a mathematical procedure called regularisation is used. In this technique solutions for which the error term drops below a predefined minimum value are calculated. A penalty term is included in the minimisation process. Physical constraints to the solution are incorporated in a penalty term. A more detailed account on the different mathematical techniques employed to provide a solution to this ill-posed problem was provided by Ansmann and Müller (2005).

The minimum number of required wavelengths for particle characterisation[1] is three, but the accuracy of the results increases if backscattering coefficients measured at up to six wavelengths are used. To account for non-spherical geometries in the retrieval it is required to include measurements of the depolarisation ratio in the retrieval process.

Modern groundbased lidar systems routinely provide measurements of the backscattering coefficients at three wavelengths and the extinction-to-backscatter ratio at two wavelengths. This type of lidar system is referred to as $3\beta+2\alpha$ system. If measurements of the depolarisation ratio at one wavelength are added the system is called $3\beta+2\alpha+1\delta$. Adding the depolarisation ratio can currently allow to retrieve information on non-spherical geometries. This was especially tested for mineral dust aerosol with spheroidal shapes (Ansmann and Müller 2005). As Raman lidars

[1]The term particle characterisation refers to the retrieval of complex refractive index, effective radius, as well as volume, surface-area, and number concentrations.

and HSRL both commonly use Nd:YAG probed lasers (Eloranta 2005; Wandinger 2005) those wavelengths are typically 355 nm, 532 nm, and 1064 nm. Until recently it was not possible to measure the extinction coefficient at 1064 nm (Haarig et al. 2018, 2016). A study on the information content of depolarisation ratio in complex microphysical aerosol retrievals recommends the use at 355 nm and, if possible, at 532 nm, under the assumption of spheroidal dust particles (Tesche et al. 2019).

Chapter 4

Optical properties and atmospheric radiative transfer

Both active and passive remote sensing involve interaction of particles with electromagnetic waves as well as the propagation of electromagnetic radiation through the atmosphere.

The electromagnetic field in absence of any particle is referred to as incident field. The presences of particles, which interact with the electromagnetic field, causes changes in the electromagnetic field. This change of the total electromagnetic field is called electromagnetic scattering. The difference between the altered (total) and the unaltered (incident) field is the scattered field (Mishchenko 2009).

The changes of the electromagnetic field caused by particles can be quantified with the help of various different optical parameters. These quantities themselves are required for radiative transfer calculations, which describe the propagation of electromagnetic radiation through the atmosphere. Both optical properties and radiative transfer calculations provide a framework to describe and interpret applications such as remote sensing and radiative forcing calculations.

Section 4.1 of this chapter is largely based on the work by Bohren and Huffman (1983) and Mishchenko et al. (2002) and will give a very brief overview on single scattering properties. Section 4.2 is mainly based on Zdunkowski et al. (2007) and aims to introduce basic concepts of atmospheric radiative transfer.

4.1 Optical properties

Transport of electromagnetic energy in an homogeneous medium without sources can be described by plane electromagnetic waves (Mishchenko et al. 2002):

$$\vec{E} = \vec{E}_0 \exp\left(-\vec{k}_I \cdot \vec{r}\right) \exp\left(i\vec{k}_R \cdot \vec{r} - i\omega t\right) \tag{4.1}$$

$$\vec{H} = \vec{H}_0 \exp\left(-\vec{k}_I \cdot \vec{r}\right) \exp\left(i\vec{k}_R \cdot \vec{r} - i\omega t\right) \tag{4.2}$$

Here $\vec{E}$ is the electric field vector and $\vec{H}$ the magnetic field vector. $\vec{E}_0 \exp\left(-\vec{k}_I \cdot \vec{r}\right)$ and $\vec{H}_0 \exp\left(-\vec{k}_I \cdot \vec{r}\right)$ respectively are the amplitudes of the electric and the magnetic waves and the phase of both waves is defined by $i\vec{k}_R \cdot \vec{r} - i\omega t$.

The time rate of the flow of electromagnetic energy per unit area is described by the Poynting vector (Zdunkowski et al. 2007), which can be calculated as the vector product of the electric field vector $\vec{E}$ and the magnetic field vector $\vec{H}$ (Bohren and Huffman 1983):

$$\vec{S} = \vec{E} \times \vec{H} \tag{4.3}$$

The magnitude of the time-averaged Poynting vector is the irradiance.

Now a single arbitrary particle embedded in a non-absorbing medium is considered and an imaginary sphere of radius r is constructed around the particle. The net rate at which electromagnetic energy crosses the surface A of this imaginary sphere is calculated with the help of the Poynting vector and the unit vector in direction of r $\hat{e}_r$.

$$W_A = -\int_A \vec{S} \cdot \hat{e}_r dA \tag{4.4}$$

This net rate of energy crossing the surface W_A corresponds to the energy remaining within the particle and thus being the absorbed radiant energy flux W_{abs}. Under the assumption of a harmonic field, Poynting vectors for the extinction $\vec{S}_{ext}$ and the scattering component $\vec{S}_{sca}$ can be derived. With the help of these Poynting vectors the net energy rate corresponding to extinction W_{ext} and the scattering W_{sca} can be calculated:

$$W_{\text{sca}} = \int \vec{S}_{\text{sca}} \cdot \hat{e}_r dA \tag{4.5}$$

$$W_{\text{ext}} = -\int_A \vec{S}_{\text{ext}} \cdot \hat{e}_r dA \tag{4.6}$$

With the help of various algebraic transformations it can be shown (for derivation see Bohren and Huffman (1983)), that in case of unpolarised incident light the optical cross sections can be obtained by dividing the respective radiant energy fluxes by the incident irradiance I_i.

$$C_{\text{ext}} = \frac{W_{\text{ext}}}{I_i} \tag{4.7}$$

$$C_{\text{abs}} = \frac{W_{\text{abs}}}{I_i} \tag{4.8}$$

$$C_{\text{sca}} = \frac{W_{\text{sca}}}{I_i} \tag{4.9}$$

From conservation of energy follows that the extinction cross section C_{ext} is equal to the sum of absorption C_{abs} and scattering cross section C_{sca}:

$$C_{\text{ext}} = C_{\text{abs}} + C_{\text{sca}} \tag{4.10}$$

The optical cross sections may be normalised by the particle's cross sectional area G projected onto a plane perpendicular to the incident beam. These normalised quantities are referred to as optical efficiencies Q. (Despite the name the optical efficiencies may be larger than unity.)

$$Q_{\text{ext}} = \frac{C_{\text{ext}}}{G} \tag{4.11}$$

$$Q_{\text{abs}} = \frac{C_{\text{abs}}}{G} \tag{4.12}$$

$$Q_{\text{sca}} = \frac{C_{\text{sca}}}{G} \tag{4.13}$$

The ratio between C_{sca} and C_{ext}, and Q_{sca} and Q_{ext} respectively is called single scattering albedo (SSA, ω):

$$\omega = SSA = \frac{C_{\text{sca}}}{C_{\text{ext}}} = \frac{Q_{\text{sca}}}{Q_{\text{ext}}} \tag{4.14}$$

For $\omega = SSA = 1$ the particle is purely scattering (hence there is no absorption); correspondingly, for $\omega = SSA = 0$ the particle is purely absorbing (i.e., there is no scattering).

Electromagnetic radiation can be described by the Stokes vector (I, Q, U, V), a generalisation of irradiance and thus describing energy and polarisation[1]. The different components of the Stokes vector are I the total irradiance, Q the linearly polarised irradiance with respect to a reference plane, U the linearly polarised irradiance with respect to a plane tilted by $\pm 45°$ compared to polarisation plane and V the circularly polarised irradiance. The Stokes vector of the incident wave (I_i, Q_i, U_i, V_i) is related to the Stokes vector of the scattered wave (I_s, Q_s, U_s, V_s) by the scattering matrix. The Stokes vector of the scattered wave assuming completely random orientation of the particle can be calculated by (Bohren and Huffman 1983):

$$\begin{pmatrix} I_s \\ Q_s \\ U_s \\ V_s \end{pmatrix} = \frac{1}{k^2 r^2} \begin{pmatrix} S_{11} & S_{12} & 0 & 0 \\ S_{12} & S_{22} & 0 & 0 \\ 0 & 0 & S_{33} & S_{34} \\ 0 & 0 & -S_{34} & S_{44} \end{pmatrix} \begin{pmatrix} I_i \\ Q_i \\ U_i \\ V_i \end{pmatrix} \tag{4.15}$$

For unpolarised incident light the S_{11} element describes the angular distribution of the scattered intensity and is also referred to as scattering phase function p. In Eq. (4.15) the phase function is defined so that: $\int_{4\pi} p d\Omega = C_{\text{sca}}$. A common normalisation

[1]It should be pointed out, that the definition of the Stokes vector varies in the literature. While Bohren and Huffman (1983) consider the Stokes vector a generalisation of irradiance, Mishchenko et al. (2002) define the Stokes vector as a generalised form of radiance. Zdunkowski et al. (2007) loosly define the elements of the Stokes vector as intensities with different possible units. As a consequence Zdunkowski et al. (2007) define the Stokes vector elements with a conversion factor carrying the units required for the intended conversion. Here the terminology follows Bohren and Huffman (1983).

of the phase function is $\int_{4\pi} p d\Omega = 1$. Usually the scattering matrix is then called (normalised) Stokes matrix F.

With the help of the scattering matrix elements further quantities can be calculated, such as the asymmetry parameter, the linear depolarisation ratio and the extinction-to-backscatter ratio.

The asymmetry parameter (g, ASY) which describes the dominant scattering direction is calculated by:

$$g = ASY = \langle \cos\theta \rangle = \int_{4\pi} F_{11} \cos\theta \mathrm{d}\Omega \tag{4.16}$$

For isotropical scattering (i.e. the same amount is scattered into all directions) the asymmetry parameter is $g = 0$. If more light is scattered to forward direction, then $g > 0$; correspondingly, if more light is scattered in backward direction then $g < 0$.

With the help of the optical cross sections and the scattering matrix elements it is possible to calculate the lidar-measureable properties detailed in Section 3.2: extinction and backscatter coefficient, extinction-to-backscatter ratio, and linear depolarisation ratio.

The aerosol extinction coefficient can be calculated from the extinction cross section and the aerosol particle size distribution by (Gasteiger et al. 2011):

$$\alpha = \int_{r_{\min}}^{r_{\max}} C_{\mathrm{ext}}(r) n(r) \mathrm{d}r, \tag{4.17}$$

Here $r_{\min}$ and $r_{\min}$ are the lower and the upper limit of the integration, respectively.

The backscattering coefficient can be calculated by (Gasteiger et al. 2011):

$$\beta = \int_{r_{\min}}^{r_{\max}} C_{\mathrm{sca}}(r) \frac{F_{11}(r, 180°)}{4\pi} n(r) \mathrm{d}r \tag{4.18}$$

F_{11} is the (1,1)-element of the normalised Stokes matrix F and C_{sca} the scattering cross section as defined above. The product of C_{sca} and $F_{11}(180°)$ is the backscattering cross section, indicating how much of the radiation is scattered backwards.

The extinction-to-backscatter ratio is commonly employed in atmospheric lidar remote sensing and sometimes referred to as lidar ratio. In measurement applications the extinction to backscatter ratio S_p is calculated by $S_p = \frac{\alpha}{\beta}$. Both the extinction coefficient α and the backscattering coefficient β depend on the total number of particles. For individual particles S_p can be calculated as:

$$S_p = LR = 4\pi \frac{C_{\mathrm{ext}}}{C_{\mathrm{sca}} F_{11}(180°)} \tag{4.19}$$

As briefly mentioned in Section 3.2 the interaction of electromagnetic radiation with particles can change its polarisation state. Highly polarised electromagnetic radiation, as employed in active remote sensing applications (see section 3.2), can become depolarised. The linear depolarisation ratio is the ratio between cross- and parallel-polarised component of the scattered radiation (Mishchenko and Hovenier

1995). For all directions and totally random orientation it is calculated by (Schnaiter et al. 2012; Takano and Jayaweera 1985):

$$\delta_l = \frac{S_{11} - S_{22}}{S_{11} \pm 2S_{12} + S_{22}} \tag{4.20}$$

The sign in the $\pm 2S_{12}$ term is determined by the incident polarisation: for horizontally polarised incident light the plus sign is to be used and for vertically polarised the minus sign is to be used.

As for $\vartheta = 180°$ $S_{12} = 0$ this expression becomes in the backscattering direction (Mishchenko and Hovenier 1995):

$$\delta_l = LDR = \left.\frac{S_{11} - S_{22}}{S_{11} + S_{22}}\right|_{\vartheta=180°} \tag{4.21}$$

In backscattering direction the linear depolarisation ratio is independent of the polarisation of the incident light. The linear depolarisation ratio is zero for spherically symmetric particles, since in that case $S_{11} = S_{22}$. Thus non-zero values of the linear depolarisation ratio indicate a deviation from spherical symmetry, either in shape or in composition. For small deviations from a spherical shape the values in the depolarisation ratio can be largest (Bi et al. 2018).

4.2 Atmospheric Radiative Transfer

Radiative transfer refers to the propagation of electro-magnetic radiation in the atmosphere. So it covers a wide range of applications from various remote sensing techniques, temperature forecasting to energy balance calculations.

Fig. 4.1 shows the incoming solar irradiance at the top of the atmosphere (grey) and at the surface (black). The differences between the two lines are caused by molecular absorption. The spectra were obtained using the radiative transfer software package libRadtran (Emde et al. 2016; Mayer and Kylling 2005) in conjunction with the radiative transfor solver DISORT and the REPTRAN parametrisation for molecular absorption (Gasteiger et al. 2014).

The propagation of electromagnetic radiation through a medium along a direction of propagation can be described by the radiative transfer equation (Eq. (4.22)).

The standard form of the radiative transfer equation for a three-dimensional medium (Zdunkowski et al. 2007) which is an integro-differential equation for radiance I_ν is:

$$-\frac{1}{k_{ext,\nu}}\Omega \cdot \nabla I_\nu = I_\nu - \frac{\omega_\nu}{4\pi}\int_{4\pi} p(\vartheta) I_\nu(\Omega')\mathrm{d}\Omega' - \frac{1}{k_{ext,\nu}} J_\nu^e \tag{4.22}$$

Here J_ν^e is the source function for true emission with units of $(\mathrm{W\,m^{-3}\,sr^{-1}\,Hz^{-1}})$ and $k_{ext,\nu}$ is the extinction coefficient. Ω is direction of propagation and ω is the single scattering albedo as defined in Eq. (4.14). p is the normalised scattering phase function with $\int_{4\pi} p\mathrm{d}\Omega' = 1$ and thus, $p = F_{11}$.

The radiative transfer equation describes sources and sinks of radiation. The first term $-\frac{1}{k_{ext,\nu}}\Omega \cdot \nabla I_\nu$ describes the loss of radiation by absorption and by scattering out

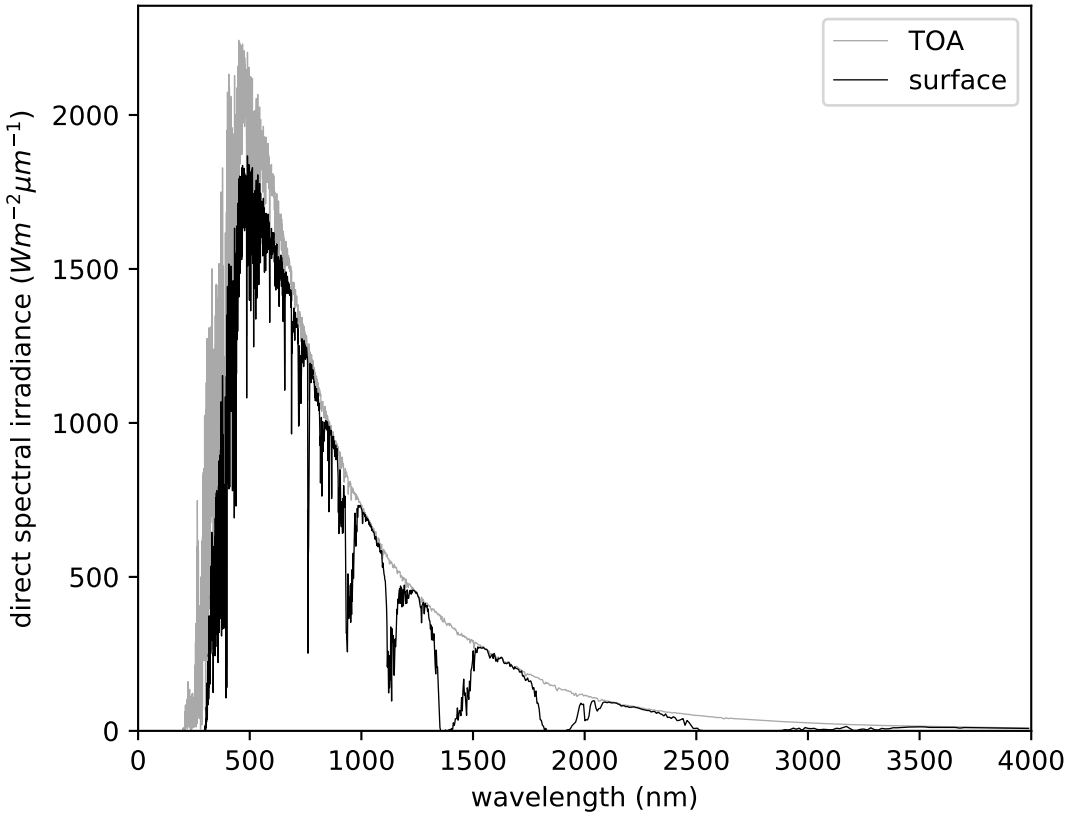

Figure 4.1: Incoming solar irradiance with a solar zenith angle of 0° at the top of atmosphere (TOA) and the surface. The spectra were obtained using the software package libRadtran.

of the direction of propagation. As previously mentioned this combination is referred to as extinction. The second term $\frac{\omega_\nu}{4\pi}\int_{4\pi} p(\vartheta)I_\nu(\Omega')\mathrm{d}\Omega'$ describes the scattering of radiation into the direction of propagation. The emission of radiation is described by the last term $\frac{1}{k_{ext,\nu}}J^e_\nu$. The emission source term in Eq. (4.22) implicitly assumes local thermodynamic equilibrium (i.e. J^e_ν should be proportional to the Planck black body function) and therefore, is restricted to the troposphere and the stratosphere.

As integro-differential equations are difficult to solve, there are a number of approximations to the radiative transfer equation. The different solving methods of the radiative transfer equation are discussed in (Zdunkowski et al. 2007). The choice of an appropriate method depends partly on the intended application. For example emission of radiation can be neglected for short wavelengths (i.e. in the solar spectrum).

4.3 Scattering solvers

There are different numerical techniques to obtain the scattering matrix (see Eq. (4.15)) and the optical cross sections.

The description of the scattering of plane waves by spherical scatterers is referred to as Mie theory (Hergert and Wriedt 2012), based on the mathematically rigorous description by Mie (1908). The Mie formulas are an exact solution to Maxwell's equations.

For particles much smaller than the wavelength of the incident radiation (with a size parameter $x = \frac{2\pi r_{eff}}{\lambda} \ll 1$) electromagnetic scattering can be approximated by Rayleigh scattering while for particles much larger than the wavelength ($x \gg 1$) geometric optics serves as a suitable approximation (Bohren and Huffman 1983).

Modifications allow for applying the Mie theory to other types of spheres such as coated spheres, spheres in an absorbing medium or magnetic spheres (Hergert and Wriedt 2012). Only the former type is of relevance for modelling soot aerosol (see Chapter 5).

In case of non-spherical particles different methods are employed to solve the scattering problem. An overview of numerical methods can be found in (Kahnert 2016).

Highly accurate results can be obtained by the T-matrix method, first proposed by (Waterman 1965). The T-matrix only depends on the particle's shape and size, the refractive index and the incident wavelength. Symmetries, especially axial symmetries drastically reduce the computation time required (Kahnert 2016). Treating particles consisting of multiple spheres with the T-matrix formalism can be considered an extension of the Mie theory. A generalized account on obtaining scattering and optical properties from multiple spheres with the T-matrix formulation, which results in an implicit mathematical description of the scattered field and hence requires numerical methods is presented by Hergert and Wriedt (2012). A more detailed account on the T-matrix method and how to calculate the scattering matrix from the T-matrix can be found in (Mishchenko et al. 2002). This method is frequently used to calculate the optical properties of soot containing aerosol (e.g., Kahnert 2017; Liu et al. 2017a; Liu and Mishchenko 2018; Luo et al. 2018; Mishchenko et al. 2016, 2013)

The discrete dipole approximation (DDA) proposed by Purcell and Pennypacker (1973) and refined by Draine and Flatau (1994) divides the scattering particle into fully polarisable volume elements, which are smaller than the wavelength, to solve the volumetric scattering equation. The small volume elements interact with each other and the incident field. This results into a set of linear equations. These equations are solved using standard numerical techniques. By dividing the scatterer into small dipoles arbitrarily shaped scatterers can be considered. Since the complex refractive index is associated to the polarisability of each dipole individually, inhomogeneities within single particles can be considered as well. Further account on the DDA method is provided by Yurkin and Hoekstra (2007, 2011). The DDA is another technique commonly used to calculate the optical properties of soot particles (e.g,

Adachi et al. 2010; Doner and Liu 2017; Doner et al. 2017; Ishimoto et al. 2019; Kahnert 2017; Liu et al. 2016).

Usually the choice of the solving method of the scattering problem and the choice of the particle model are linked to each other: The Mie theory requires spherical models, while particle models with symmetries are suited for the T-matrix method, and arbitrarily shaped particle models can be used in combination with the DDA.

Chapter 5

Soot aerosol models

Soot or black carbon particles are formed in flames during combustion processes. They are characterised by the four following physical properties: strongly light-absorbing, refractory (i.e. retaining the basic form at high temperatures), water-insoluble, and they exist as aggregates of small carbonaceous spherules (Bond et al. 2013).

As soot containing aerosol particles have an important influence on the Earth's climate as well as have adverse impacts on human health, there have been various attempts to model optical properties of soot particles. There are two main uses of the optical models: to assess soot containing aerosol impact on the climate and to improve the interpretation and use of remote sensing data.

Applications in climate models rely particularly on the (mass) absorption cross section[1], the single scattering albedo and the asymmetry parameter. For remote sensing applications knowledge of the linear depolarisation ratio and the extinction-to-backscatter ratio are of use. Therefore, both applications require information on the scattering matrix, especially the scattering phase function, and the optical cross sections.

Integral properties, such as optical cross sections, asymmetry parmeter, and single scattering albedo, can be modelled with comparatively simple models. Differential properties on the other hand require more detailed models (Kahnert et al. 2013). Highly complex models, however, are in general computionally more demanding than simpler models. Thus particle models necessarily require simplifications, whether they are intended for use in climate modelling or in remote sensing retrievals (Kahnert et al. 2014). Highly complex soot models are, for example, very unlikely to be directly employed in climate modelling (Bond and Bergstrom 2006).

Various modelling studies attempt to find important morphological parameters, which have a considerable effect of the optical properties. These parameters can then be either included in the further models (e.g., Kahnert 2017) or accounted for by using correction factors (e.g., Adachi et al. 2010; Teng et al. 2019).

[1]The mass absorption cross section of a particle is calculated by dividing C_{abs} with the black carbon mass (Bond and Bergstrom 2006) or, although less commonly used, by the particle's total mass (Wu et al. 2017).

5.1 Bare (uncoated) soot patricles

Bare or uncoated soot particles can be described as fractal aggregates of N spherical monomers with radius a following a fractal scaling relation (Sorensen 2001):

$$N = k_0 \left(\frac{R_g}{a}\right)^{D_f} \tag{5.1}$$

k_0 denotes a fractal pre-factor, which describes how densely the monomers are packed along an existing branch. The fractal dimension D_f indicates the compactness of an aggregate, linearly aligned monomers would give $D_f = 1$ and a sphere would result in $D_f = 3$. Lab measurements indicate a range of $1.5 \leq D_f \leq 3.0$ for soot aggregates depending on the fuel type (Xiong and Friedlander 2001).

The radius of gyration is usually defined as R_g (Sorensen 2001):

$$R_g = \sqrt{\frac{1}{N}\sum_{i=1}^{N} |\vec{r_i} - \vec{r_c}|^2} \tag{5.2}$$

where $|\vec{r_i} - \vec{r_c}|$ is the distance between the ith monomer and the aggregate's centre of mass. This definition of the radius of gyration implicitely assumes that the different monomers are equal in mass. For different monomer masses m_i the radius of gyration is defined as (Eggersdorfer and Pratsinis 2012):

$$R_g = \sqrt{\frac{\sum_{i=1}^{N} |\vec{r_i} - \vec{r_c}|^2 m_i}{\sum_{i=1}^{N} m_i}} \tag{5.3}$$

In case of monomers of different mass, these monomers are usually polydisperse. In such a case the monomer radius a in Eq. (5.1) has to be replaced with the geometric mean radius of the monomers (Eggersdorfer and Pratsinis 2012).

Figure 5.1: Example of aggregates with $N = 64$, $k_0 = 0.7$, $D_f = 1.8$ (left), and $D_f = 2.8$ (right) obtained with an aggregation algorithm

Two examples of monodisperse model aggregates consisting of 64 monomers with a fractal prefactor of $k_0 = 0.7$ and fractal dimensions of $D_f = 1.8$ (left), and $D_f = 2.8$ (right) respectively, are shown in Fig. 5.1. Both aggregates were constructed using

an aggregation algorithm, which builds the aggregate from smaller aggregates and individual monomers, so that Eq. (5.1) is fulfilled at every step of the construction process (Mackowski 2006). It can be seen, that the aggregate with smaller fractal dimension is less compact, then the aggregate with the higher fractal dimension.

Effects of differences in fractal dimension and the refractive index of soot on optical cross section and asymetry parameter were investigated by Liu et al. (2008).

The assumption that fractal aggregates consist of equally-sized monomers is already a simplification compared to soot aggregates analysed in lab studies. The impact of polydisperse monomers was investigated by Doner and Liu (2017) and Liu et al. (2015a).

Aggregation algorithms produce aggregates according to the fraqctal scaling relation in Eq. (5.1). The monomers in the resulting aggregates are in point-contact, which reflects physical processes like coagulation during the aggregate formation. Chemical sintering can increase the contact between two neighbouring monomers (Brasil et al. 1999; Eggersdorfer et al. 2012). This can be understood as overlapping monomers. Overlapping monomers in bare aggregates were investigated by Doner and Liu (2017), Skorupski and Mroczka (2014), and Yon et al. (2015).

In a study by Teng et al. (2019) the impacts of deviations on optical cross sections from an idealised, bare monodisperse fractal aggregate were investigated. These deviations are polydispersity of the monomers, very thin non-absorbing coating, monomer surface irregularities, overlap and necking. Necking describes the process of adding additional material to create a smooth transition between neighbouring monomers. Of the deviations from the idealised, monodisperse aggregate necking was found to have the largest impact. The changes in optical properties were mainly driven by changes in the black carbon mass. Single scattering albedo, scattering and absorption cross section and asymmetry parameter can be corrected for not considering the deviations by multiplying a correction factor of 1.05.

5.2 Coated aggregates

Atmospheric soot particles are commonly coated by non-absorbing or weakly absorbing material, which condenses onto the aggregate (Adachi and Buseck 2008; Zhang et al. 2008). The process of material condensing happens rapidly, and thickly coated particles are predominant as is indicated by in-situ measurements (Adachi and Buseck 2008; Adachi et al. 2010; China et al. 2013; Worringen et al. 2008).

Images obtained with transmission electron microscopy (TEM) were reported by Johnson et al. (2005). These images indicate that there are two mechanisms which can result in internal mixtures of soot and non-absorbing or weakly absorbing material: coagulation and condensation.

If coating material condenses onto a soot aggregate, the aggregate's structure changes, i.e. the aggregate becomes more compact. How fast the aggregate collapses, differs depending on the coating material (Bambha et al. 2013; Ghazi and Olfert 2013; Pei et al. 2018; Schnitzler et al. 2014; Zhang et al. 2008). This compaction is reflected in an increase in the aggregate's fractal dimension D_f.

As soot aggregates in the atmosphere are commonly mixed with non- or lightly absorbing material numerical investigations require parametrisations of these mixtures. Here only internal mixtures, i.e., mixtures within the same particle, are considered.

Comparing more complex models to simplified models allows to gain insights on potential biases and uncertainties introduced by simplifications. The radiative forcing impacts of soot aerosol calculated in global climate models usually use spherical models (Adachi et al. 2010; Bond et al. 2013).

In case of modelling the optical cross sections one key property appears to be the amount of soot interacting with electromagnetic radiation: In so-called core shell models, in which the coated soot particle is parametrised as a spherical soot core embedded in a spherical shell of coating material, much of the soot inside the core is shielded from electromagnetic radiation (Kahnert et al. 2013). A similar shielding effect can be observed in open cell models, which add coating monomers to an existing soot aggregate (He et al. 2015; Liou et al. 2011). Another type of model capable of increasing the amount of soot interacting with electromagnetic radiation is the closed cell model, in which each monomer of a soot aggregate is embedded in a spherical coating shell, without altering the fractal parameters of the aggregate otherwise (He et al. 2015; Kahnert 2017; Liou et al. 2011; Liu and Mishchenko 2018; Luo et al. 2018; Mishchenko et al. 2016; Wu et al. 2014). Such closed cell models do not suffer from shielding too much soot from electromagnetic radiation (He et al. 2015). Most closed cell models assume the soot monomer and its coating shell having their respective centre at the same location, however, shifting the centre of the soot monomer with respect to the centre of coating shell does not alter the optical properties obtained from closed-cell models (Luo et al. 2018).

Several other studies based on more complex models (Adachi et al. 2010; Doner et al. 2017; Dong et al. 2015; Liu et al. 2016; Wu et al. 2017) and 3D scans of sampled soot aerosol particles (Adachi et al. 2010) highlighted the risk of homogeneous spheres and core-shell geometries misrepresenting the optical cross sections. Among the factors influencing the optical cross sections are the aggregate structure (lacy or compact) (Adachi et al. 2010; Wu et al. 2017), necking and overlapping of monomers (Doner et al. 2017), off-centre positioning of the aggregate inside the coating (Adachi et al. 2010).

The linear depolarisation ratio (see Eqs. (4.20) and (4.21)) is highly sensitive to changes of scattering particle's morphology. Studies such as Bi et al. (2018) and Mishchenko and Sassen (1998) indicate, that the depolarisation ratio is potentially oversensitive to shape changes. In addition to the shape-dependence the depolarisation ratio is sensitive to particle inohomogeneities (Kahnert 2015). As the linear depolarisation ratio is zero for spherically symmetric particles, core-shell models cannot be used for modelling linear depolarisation ratios. As a result modelling linear depolarisation ratio requires non-spherical particle geometries. In case of mineral dust aerosol, which is usually highly non-spherical, the linear depolarisation ratio is frequently modelled with the help of spheroidal geometries (e.g, Gasteiger et al. 2011; Mishchenko et al. 1997; Wiegner et al. 2009). By changing the ratio of the axes of a spheroid the model geometry can be fitted to a large range of observed linear depolarisation ratios. Mishchenko et al. (2016) used a coated spheroid model to

model linear depolarisation ratios. While this coated spheroid model can reproduce lidar field measurements, it provides only limited insight into the relation between morphological and optical properties.

For modelling optical cross sections the open cell model posed less risk of underestimating cross sections than the core-shell model, as mentioned above. In case of modelling the linear depolarisation ratio it poses, however, the risk of underestimating the depolarisation ratio of thickly coated aggregates (Kahnert 2017; Liu and Mishchenko 2018).

Large volumes of coating material are frequently parametrised as spheres, in which an aggregate is inserted (reflecting condensation) or attached (reflecting coagulation). These parmetrisations are based on insights obtained from TEM images. A stronger focus of previous studies was the modelling of optical cross sections, the respective optical efficiencies, asymmetry parameter and single scattering albedo (Dong et al. 2015; Liu et al. 2017b; Wu et al. 2016, 2015). The optical cross sections are insensitive to wheater or not the surfaces of the monomers intersecting with the surface of the spherical coating or not (Wu et al. 2015). The depolarisation ratio of soot with spherical coating was investigated by Liu and Mishchenko (2018) and Mishchenko et al. (2016).

Kahnert (2017) proposed a coating model, which adds coating layer by layer onto an aggregate. The coating follows the shape of the aggregate constrained by a sphere with the aggregate's maximum dimension as diameter. After this sphere is filled the coating layers are added radially.

By defining an artificial surface tension a coating algorithm mimicking physical processes is proposed by Ishimoto et al. (2019). This artificial surface tension results in the particles becoming gradually more spherical with increasing amount of coating material.

Both studies (Ishimoto et al. 2019; Kahnert 2017) indicate that particle models which result in spherical coatings only for rather low soot volume fractions, i.e. thick coatings, pose the risk of overestimating depolarisation ratios.

To avoid such risk of overestimating depolarisation ratios, a particle model, which allows for the coating becoming spherical at higher soot volume fraction, is required. Such a model is then expected to reduce the risk of overestimating the modelled linear depolarisation ratios.

Chapter 6

Summary and Outlook

6.1 Appended publications

Paper A

In Paper A a soot coating model with a tunable transition between surface film coating and spherical shell coating is introduced. The proposed coating mechanism is strongly connected to the use of the DDA since the coating material is added dipole by dipole until a predefined soot volume fraction is reached. The coating follows the shape of the bare aggregate but is at first constrained by a sphere. After this constraining sphere is filled, the coating material is added radially onto the sphere. The diameter of the sphere is determined by the largest dimension of the soot aggregate and multiplied with a dimensionless free scaling parameter f_c. Two model configurations are compared with each other: $f_c = 1$ and $f_c = 0.6$. The former configuration poses the risk of overestimating values of the linear depolarisation ratio. Different sources of uncertainty were assessed: different stochastic realisations of the fractal aggregate, changes in refractive index of both coating and aggregate, overlapping between monomers, uncertainties in the fractal parameters k_0, D_f and a_{mon} (the latter in conjunction with changes in monomer number).

Paper B

Paper B builds on the uncertainty estimate in Paper A in which the depolarisation ratio was found be highly sensitive to changes in the refractive index. In Paper B the possibility to distinguish two different coating materials (sulphate coating and toluene-based coating) using the depolarisation ratio, the extinction-to-backscatter ratio and the aerosol particle's Ångström exponents are investigated. The Ångström exponent allows to quantify changes of the backscattering coefficient, the extinction coefficient and the extinction-to-backscatter ratio between two wavelengths. The scattering particles were obtained using the model presented in Paper A. The differences in optical properties potentially allow for the distinction of coating materials using lidar measurements.

6.2 Outlook

The model presented in Paper A requires a comparison with laboratory measurements, which goes beyond the consistency check with lidar field measurements already presented. Lab measurements which provide both optical properties as well as a microphysical characterisation of the particles can help to constrain the model. Furthermore, after having the model constrained by lab measurements, a more in-depth comparison with remote sensing data could be attempted.

While the sulphate coating assumed in Paper B can be considered representative for inorganic coating materials with respect to the dielectric properties (Adachi et al. 2010), the toluene-based coating is not necessarily representative for organic coatings. The dielectric properties of organic coating material (reflected by the complex refractive index) depend on the precursor material and the reaction conditions (Liu et al. 2015b; Liu et al. 2013). In a follow-up study differences in the optical properties induced by different organic coating materials can be investigated. Another follow-up study to Paper B could investigate how the differences in depolarisation ratio and extinction-to-backscatter ratio translate into microphysical retrievals used for lidar measurements by producing synthetic lidar measurements.

Bibliography

Adachi, K. and P. R. Buseck (2008). "Internally mixed soot, sulfates, and organic matter in aerosol particles from Mexico City". *Atmos. Chem. Phys.* 8.21, pp. 6469–6481. DOI: 10.5194/acp-8-6469-2008 (cit. on p. 27).

Adachi, K., S. H. Chung, and P. R. Buseck (2010). "Shapes of soot aerosol particles and implications for their effects on climate". *J. Geophys. Res.* 115.D15, n/a–n/a. DOI: 10.1029/2009JD012868 (cit. on pp. 23, 25, 27, 28, 32).

Anenberg, S. C., K. Talgo, S. Arunachalam, P. Dolwick, C. Jang, and J. J. West (2011). "Impacts of global, regional, and sectoral black carbon emission reductions on surface air quality and human mortality". *Atmos. Chem. Phys.* 11.14, pp. 7253–7267. DOI: 10.5194/acp-11-7253-2011 (cit. on pp. 3, 10).

Anenberg, S. C., J. Schwartz, D. Shindell, M. Amann, G. Faluvegi, Z. Klimont, G. Janssens-Maenhout, L. Pozzoli, R. Van Dingenen, E. Vignati, L. Emberson, N. Z. Muller, J. J. West, M. Williams, V. Demkine, W. K. Hicks, J. Kuylenstierna, F. Raes, and V. Ramanathan (2012). "Global Air Quality and Health Co-benefits of Mitigating Near-Term Climate Change through Methane and Black Carbon Emission Controls". *Environ. Health Perspect.* 120.6. DOI: 10.1289/ehp.1104301 (cit. on pp. 3, 10).

Ansmann, A. and D. Müller (2005). "Lidar and Atmospheric Aerosol Particles". In: *Lidar*. Ed. by C. Weitkamp. Vol. 102. Springer Series in Optical Sciences. Springer, New York, NY, pp. 105–141. DOI: 10.1007/0-387-25101-4_4 (cit. on pp. 11–15).

Bambha, R. P., M. A. Dansson, P. E. Schrader, and H. A. Michelsen (2013). "Effects of volatile coatings and coating removal mechanisms on the morphology of graphitic soot". *Carbon* 61, pp. 80–96. ISSN: 0008-6223. DOI: 10.1016/j.carbon.2013.04.070 (cit. on p. 27).

Bi, L., W. Lin, D. Liu, and K. Zhang (2018). "Assessing the depolarization capabilities of nonspherical particles in a super-ellipsoidal shape space". *Opt. Express* 26.2, pp. 1726–1742. DOI: 10.1364/OE.26.001726 (cit. on pp. 21, 28).

Bohren, C. F. and D. R. Huffman (1983). *Absorption and scattering of light by small particles*. Wiley New York. ISBN: 978-0-471-29340-8 (cit. on pp. 17–19, 23).

Bond, T. C., S. J. Doherty, D. W. Fahey, P. M. Forster, T. Berntsen, B. J. DeAngelo, M. G. Flanner, S. Ghan, B. Kärcher, D. Koch, S. Kinne, Y. Kondo, P. K. Quinn, M. C. Sarofim, M. G. Schultz, M. Schulz, C. Venkataraman, H. Zhang, S. Zhang, N. Bellouin, S. K. Guttikunda, P. K. Hopke, M. Z. Jacobson, J. W. Kaiser, Z. Klimont, U. Lohmann, J. P. Schwarz, D. Shindell, T. Storelvmo, S. G. Warren, and C. S. Zender (2013). "Bounding the role of black carbon in the climate

system: A scientific assessment". *J. Geophys. Res.* 118.11, pp. 5380–5552. DOI: 10.1002/jgrd.50171 (cit. on pp. 3, 10, 25, 28).

Bond, T. C. and R. W. Bergstrom (2006). "Light Absorption by Carbonaceous Particles: An Investigative Review". *Aerosol Sci. Technol.* 40.1, pp. 27–67. DOI: 10.1080/02786820500421521 (cit. on p. 25).

Boucher, O. (2015). *Atmospheric Aerosols - Properties and Climate Impacts*. Springer, Dordrecht. ISBN: 978-94-017-9649-1. DOI: 10.1007/978-94-017-9649-1 (cit. on pp. 7–9, 11, 12).

Brasil, A., T. Farias, and M. Carvalho (1999). "A RECIPE FOR IMAGE CHARACTERIZATION OF FRACTAL-LIKE AGGREGATES". *J. Aerosol Sci.* 30.10, pp. 1379–1389. DOI: 10.1016/S0021-8502(99)00026-9 (cit. on p. 27).

Casadevall, T. J. (1994). "The 1989–1990 eruption of Redoubt Volcano, Alaska: impacts on aircraft operations". *J. Volcanol. Geotherm. Res.* 62.1. The 1989-1990 Eruptions of Redoubt Volcano, Alaska, pp. 301–316. ISSN: 0377-0273. DOI: 10.1016/0377-0273(94)90038-8 (cit. on p. 9).

China, S., C. Mazzoleni, K. Gorkowski, A. C. Aiken, and M. K. Dubey (2013). "Morphology and mixing state of individual freshly emitted wildfire carbonaceous particles". *Nat. Commun.* 4.2122. DOI: 10.1038/ncomms3122 (cit. on p. 27).

Doner, N. and F. Liu (2017). "Impact of morphology on the radiative properties of fractal soot aggregates". *J. Quant. Spectrosc. Radiat. Transfer* 187.Supplement C, pp. 10–19. ISSN: 0022-4073. DOI: 10.1016/j.jqsrt.2016.09.005 (cit. on pp. 24, 27).

Doner, N., F. Liu, and J. Yon (2017). "Impact of necking and overlapping on radiative properties of coated soot aggregates". *Aerosol Sci. Technol.* 51.4, pp. 532–542. DOI: 10.1080/02786826.2016.1275513 (cit. on pp. 24, 28).

Dong, J., J. Zhao, and L. Liu (2015). "Morphological effects on the radiative properties of soot aerosols in different internally mixing states with sulfate". *J. Quant. Spectrosc. Radiat. Transfer* 165.Supplement C, pp. 43–55. DOI: 10.1016/j.jqsrt.2015.06.025 (cit. on pp. 28, 29).

Draine, B. T. and P. J. Flatau (1994). "Discrete-Dipole Approximation For Scattering Calculations". *J. Opt. Soc. Am. A* 11.4, pp. 1491–1499. DOI: 10.1364/JOSAA.11.001491 (cit. on p. 23).

Eggersdorfer, M. L. and S. Pratsinis (2012). "The Structure of Agglomerates Consisting of Polydisperse Particles". *Aerosol Sci. Technol.* 46.3, pp. 347–353. DOI: 10.1080/02786826.2011.631956 (cit. on p. 26).

Eggersdorfer, M. L., D. Kadau, H. J. Herrmann, and S. E. Pratsinis (2012). "Aggregate morphology evolution by sintering: Number and diameter of primary particles". *J. Aerosol Sci.* 46, pp. 7–19. ISSN: 0021-8502. DOI: 10.1016/j.jaerosci.2011.11.005 (cit. on p. 27).

Eloranta, E. E. (2005). "High Spectral Resolution Lidar". In: *Lidar: Range-Resolved Optical Remote Sensing of the Atmosphere*. Ed. by C. Weitkamp. New York, NY: Springer New York, pp. 143–163. ISBN: 978-0-387-25101-1. DOI: 10.1007/0-387-25101-4_5 (cit. on p. 16).

Emde, C., R. Buras-Schnell, A. Kylling, B. Mayer, J. Gasteiger, U. Hamann, J. Kylling, B. Richter, C. Pause, T. Dowling, and L. Bugliaro (2016). "The libRadtran

software package for radiative transfer calculations (version 2.0.1)". *Geosci. Model Dev.* 9.5, pp. 1647–1672. DOI: 10.5194/gmd-9-1647-2016 (cit. on p. 21).

Freudenthaler, V. (2016). "About the effects of polarising optics on lidar signals and the Δ90 calibration". *Atmos. Meas. Tech.* 9.9, pp. 4181–4255. DOI: 10.5194/amt-9-4181-2016 (cit. on p. 13).

Freudenthaler, V., M. Esselborn, M. Wiegner, B. Heese, M. Tesche, A. Ansmann, D. Müller, D. Althausen, M. Wirth, A. Fix, G. Ehret, P. Knippertz, C. Toledano, J. Gasteiger, M. Garhammer, and M. Seefeldner (2009). "Depolarization ratio profiling at several wavelengths in pure Saharan dust during SAMUM 2006". *Tellus B* 61.1, pp. 165–179. ISSN: 1600-0889. DOI: 10.1111/j.1600-0889.2008.00396.x (cit. on pp. 13, 14).

Gasteiger, J., C. Emde, B. Mayer, R. Buras, S. Buehler, and O. Lemke (2014). "Representative wavelengths absorption parameterization applied to satellite channels and spectral bands". *J. Quant. Spectrosc. Radiat. Transfer* 148, pp. 99–115. ISSN: 0022-4073. DOI: 10.1016/j.jqsrt.2014.06.024 (cit. on p. 21).

Gasteiger, J., M. Wiegner, S. Groß, V. Freudenthaler, C. Toledano, M. Tesche, and K. Kandler (2011). "Modelling lidar-relevant optical properties of complex mineral dust aerosols". *Tellus B* 63.4, pp. 725–741. DOI: 10.1111/j.1600-0889.2011.00559.x (cit. on pp. 20, 28).

Ghazi, R. and J. S. Olfert (2013). "Coating Mass Dependence of Soot Aggregate Restructuring due to Coatings of Oleic Acid and Dioctyl Sebacate". *Aerosol Sci. Technol.* 47.2, pp. 192–200. DOI: 10.1080/02786826.2012.741273 (cit. on p. 27).

Haarig, M., A. Ansmann, H. Baars, C. Jimenez, I. Veselovskii, R. Engelmann, and D. Althausen (2018). "Depolarization and lidar ratios at 355, 532, and 1064 nm and microphysical properties of aged tropospheric and stratospheric Canadian wildfire smoke". *Atmos. Chem. Phys.* 2018.16, pp. 11847–11861. DOI: 10.5194/acp-18-11847-2018 (cit. on p. 16).

Haarig, M., R. Engelmann, A. Ansmann, I. Veselovskii, D. N. Whiteman, and D. Althausen (2016). "1064 nm rotational Raman lidar for particle extinction and lidar-ratio profiling: cirrus case study". *Atmos. Meas. Tech.* 9.9, pp. 4269–4278. DOI: 10.5194/amt-9-4269-2016 (cit. on p. 16).

He, C., K.-N. Liou, Y. Takano, R. Zhang, M. Levy Zamora, P. Yang, Q. Li, and L. R. Leung (2015). "Variation of the radiative properties during black carbon aging: theoretical and experimental intercomparison". *Atmos. Chem. Phys.* 15.20, pp. 11967–11980. DOI: 10.5194/acp-15-11967-2015 (cit. on p. 28).

Hergert, W. and T. Wriedt, eds. (2012). *The Mie Theory - Basics and Applications.* Springer, Berlin, Heidelberg. ISBN: 978-3-642-28738-1. DOI: 10.1007/978-3-642-28738-1 (cit. on p. 23).

Holton, J. R. (2004). *An Introduction to Dynamic Meteorology.* Fourth Edition. Boston: Elsevier Academic Press. ISBN: 0-12-354015-1 (cit. on pp. 5, 7).

Hoose, C., J. E. Kristjánsson, J.-P. Chen, and A. Hazra (2010). "A Classical-Theory-Based Parameterization of Heterogeneous Ice Nucleation by Mineral Dust, Soot, and Biological Particles in a Global Climate Model". *J. Atmos. Sci.* 67.8, pp. 2483–2503. DOI: 10.1175/2010JAS3425.1 (cit. on p. 9).

Ishimoto, H., R. Kudo, and K. Adachi (2019). "A shape model of internally mixed soot particles derived from artificial surface tension". *Atmos. Meas. Tech.* 12.1, pp. 107–118. DOI: 10.5194/amt-12-107-2019 (cit. on pp. 24, 29).

Johnson, K. S., B. Zuberi, L. T. Molina, M. J. Molina, M. J. Iedema, J. P. Cowin, D. J. Gaspar, C. Wang, and A. Laskin (2005). "Processing of soot in an urban environment: case study from the Mexico City Metropolitan Area". *Atmos. Chem. Phys.* 5.11, pp. 3033–3043. DOI: 10.5194/acp-5-3033-2005 (cit. on p. 27).

Kahnert, M. (2015). "Modelling radiometric properties of inhomogeneous mineral dust particles: Applicability and limitations of effective medium theories". *J. Quant. Spectrosc. Radiat. Transfer* 152, pp. 16–27. DOI: 10.1016/j.jqsrt.2014.10.025 (cit. on p. 28).

Kahnert, M. (2016). "Numerical solutions of the macroscopic Maxwell equations for scattering by non-spherical particles: A tutorial review". *J. Quant. Spectrosc. Radiat. Transfer* 178.Supplement C. Electromagnetic and light scattering by nonspherical particles XV: Celebrating 150 years of Maxwell's electromagnetics, pp. 22–37. DOI: 10.1016/j.jqsrt.2015.10.029 (cit. on p. 23).

Kahnert, M. (2017). "Optical properties of black carbon aerosols encapsulated in a shell of sulfate: comparison of the closed cell model with a coated aggregate model". *Opt. Express* 25.20, pp. 24579–24593. DOI: 10.1364/OE.25.024579 (cit. on pp. 23–25, 28, 29).

Kahnert, M., T. Nousiainen, and H. Lindqvist (2013). "Models for integrated and differential scattering optical properties of encapsulated light absorbing carbon aggregates". *Opt. Express* 21.7, pp. 7974–7993. DOI: 10.1364/OE.21.007974 (cit. on pp. 25, 28).

Kahnert, M., T. Nousiainen, and H. Lindqvist (2014). "Review: Model particles in atmospheric optics". *J. Quant. Spectrosc. Radiat. Transfer* 146.Supplement C. Electromagnetic and Light Scattering by Nonspherical Particles XIV, pp. 41–58. DOI: 10.1016/j.jqsrt.2014.02.014 (cit. on p. 25).

Liou, K., Y. Takano, and P. Yang (2011). "Light absorption and scattering by aggregates: Application to black carbon and snow grains". *J. Quant. Spectrosc. Radiat. Transfer* 112.10, pp. 1581–1594. DOI: 10.1016/j.jqsrt.2011.03.007 (cit. on p. 28).

Liu, C., J. Li, Y. Yin, B. Zhu, and Q. Feng (2017a). "Optical properties of black carbon aggregates with non-absorptive coating". *J. Quant. Spectrosc. Radiat. Transfer* 187, pp. 443–452. ISSN: 0022-4073. DOI: https://doi.org/10.1016/j.jqsrt.2016.10.023 (cit. on p. 23).

Liu, C., Y. Yin, F. Hu, H. Jin, and C. M. Sorensen (2015a). "The Effects of Monomer Size Distribution on the Radiative Properties of Black Carbon Aggregates". *Aerosol Sci. Technol.* 49.10, pp. 928–940. DOI: 10.1080/02786826.2015.1085953 (cit. on p. 27).

Liu, D., J. Whitehead, M. R. Alfarra, E. Reyes-Villegas, D. V. Spracklen, C. L. Reddington, S. Kong, P. I. Williams, Y.-C. Ting, S. Haslett, J. W. Taylor, M. J. Flynn, W. T. Morgan, G. McFiggans, H. Coe, and J. D. Allan (2017b). "Black-carbon absorption enhancement in the atmosphere determined by particle mixing

state". *Nat. Geosci.* 10. Article, pp. 184–188. DOI: 10.1038/ngeo2901 (cit. on p. 29).

Liu, F., J. Yon, and A. Bescond (2016). "On the radiative properties of soot aggregates – Part 2: Effects of coating". *J. Quant. Spectrosc. Radiat. Transfer* 172.Supplement C, pp. 134–145. DOI: 10.1016/j.jqsrt.2015.08.005 (cit. on pp. 24, 28).

Liu, L. and M. I. Mishchenko (2018). "Scattering and Radiative Properties of Morphologically Complex Carbonaceous Aerosols: A Systematic Modeling Study". *Remote Sensing* 10.10. ISSN: 2072-4292. DOI: 10.3390/rs10101634 (cit. on pp. 23, 28, 29).

Liu, L., M. I. Mishchenko, and W. P. Arnott (2008). "A study of radiative properties of fractal soot aggregates using the superposition T-matrix method". *J. Quant. Spectrosc. Radiat. Transfer* 109.15. DOI: 10.1016/j.jqsrt.2008.05.001 (cit. on p. 27).

Liu, P. F., N. Abdelmalki, H.-M. Hung, Y. Wang, W. H. Brune, and S. T. Martin (2015b). "Ultraviolet and visible complex refractive indices of secondary organic material produced by photooxidation of the aromatic compounds toluene and m-xylene". *Atmos. Chem. Phys.* 15.3, pp. 1435–1446. DOI: 10.5194/acp-15-1435-2015 (cit. on p. 32).

Liu, P., Y. Zhang, and S. T. Martin (2013). "Complex Refractive Indices of Thin Films of Secondary Organic Materials by Spectroscopic Ellipsometry from 220 to 1200 nm". *Environ. Sci. Technol.* 47.23. PMID: 24191734, pp. 13594–13601. DOI: 10.1021/es403411e (cit. on p. 32).

Luo, J., Y. Zhang, and Q. Zhang (2018). "A model study of aggregates composed of spherical soot monomers with an acentric carbon shell". *J. Quant. Spectrosc. Radiat. Transfer* 205, pp. 184–195. ISSN: 0022-4073. DOI: 10.1016/j.jqsrt.2017.10.024 (cit. on pp. 23, 28).

Mackowski, D. W. (2006). "A simplified model to predict the effects of aggregation on the absorption properties of soot particles". *J. Quant. Spectrosc. Radiat. Transfer* 100.1. VIII Conference on Electromagnetic and Light Scattering by Nonspherical Particles, pp. 237–249. DOI: 10.1016/j.jqsrt.2005.11.041 (cit. on p. 27).

Mayer, B. and A. Kylling (2005). "Technical note: The libRadtran software package for radiative transfer calculations - description and examples of use". *Atmos. Chem. Phys.* 5.7, pp. 1855–1877. DOI: 10.5194/acp-5-1855-2005 (cit. on p. 21).

Mie, G. (1908). "Beiträge zur Optik trüber Medien, speziell kolloidaler Metalllösungen". *Ann. Phys.* 330.3, pp. 377–445. DOI: 10.1002/andp.19083300302 (cit. on p. 23).

Mishchenko, M. I. and J. W. Hovenier (1995). "Depolarization of light backscattered by randomly oriented nonspherical particles". *Opt. Lett.* 20.12, pp. 1356–1358. DOI: 10.1364/OL.20.001356 (cit. on pp. 20, 21).

Mishchenko, M. I. (2009). "Gustav Mie and the fundamental concept of electromagnetic scattering by particles: A perspective". *J. Quant. Spectrosc. Radiat. Transfer* 110.14. XI Conference on Electromagnetic and Light Scattering by Non-Spherical Particles: 2008, pp. 1210–1222. ISSN: 0022-4073. DOI: 10.1016/j.jqsrt.2009.02.002 (cit. on p. 17).

Mishchenko, M. I., J. M. Dlugach, and L. Liu (2016). "Linear depolarization of lidar returns by aged smoke particles". *Appl. Opt.* 55.35. DOI: 10.1364/AO.55.009968 (cit. on pp. 23, 28, 29).

Mishchenko, M. I., L. Liu, and D. W. Mackowski (2013). "T-matrix modeling of linear depolarization by morphologically complex soot and soot-containing aerosols". *J. Quant. Spectrosc. Radiat. Transfer* 123. Peter C. Waterman and his scientific legacy, pp. 135–144. ISSN: 0022-4073. DOI: https://doi.org/10.1016/j.jqsrt.2012.11.012 (cit. on p. 23).

Mishchenko, M. I. and K. Sassen (1998). "Depolarization of lidar returns by small ice crystals: An application to contrails". *Geophys. Res. Lett.* 25.3, pp. 309–312. ISSN: 1944-8007. DOI: 10.1029/97GL03764 (cit. on p. 28).

Mishchenko, M. I., L. D. Travis, R. A. Kahn, and R. A. West (1997). "Modeling phase functions for dustlike tropospheric aerosols using a shape mixture of randomly oriented polydisperse spheroids". *J. Geophys. Res.* 102.D14, pp. 16831–16847. DOI: 10.1029/96JD02110 (cit. on p. 28).

Mishchenko, M. I., L. D. Travis, and A. A. Lacis (2002). *Scattering, Absorption, and Emission of Light by Small Particles*. CAMBRIDGE UNIVERSITY PRESS. ISBN: 9780521782524 (cit. on pp. 17, 19, 23).

Murray, B. J., O. O'Sullivan, J. D. Atkinson, and M. Webb (2012). "Ice nucleation by particles immersed in supercooled cloud droplets". *Chem. Soc. Rev.* 41, pp. 6519–6554. DOI: 10.1039/C2CS35200A (cit. on p. 9).

Myhre, G., D. Shindell, F.-M. Bréon, W. Collins, J. Fuglestvedt, J. Huang, D. Koch, J.-F. Lamarque, D. Lee, B. Mendoza, T. Nakajima, A. Robock, G. Stephens, T. Takemura, and H. Zhang (2013). "Anthropogenic and Natural Radiative Forcing". In: *Climate Change 2013: The Physical Science Basis. Contribution of Working Group I to the Fifth Assessment Report of the Intergovernmental Panel on Climate Change*. Ed. by T. Stocker, D. Qin, G.-K. Plattner, M. Tignor, S. Allen, J. Boschung, A. Nauels, Y. Xia, V. Bex, and P. Midgley. Cambridge, United Kingdom and New York, NY, USA: Cambridge University Press. Chap. 8, pp. 659–740. ISBN: ISBN 978-1-107-66182-0. DOI: 10.1017/CBO9781107415324.018 (cit. on pp. 3, 9, 10).

Pei, X., M. Hallquist, A. C. Eriksson, J. Pagels, N. M. Donahue, T. Mentel, B. Svenningsson, W. Brune, and R. K. Pathak (2018). "Morphological transformation of soot: investigation of microphysical processes during the condensation of sulfuric acid and limonene ozonolysis product vapors". *Atmos. Chem. Phys.* 18.13, pp. 9845–9860. DOI: 10.5194/acp-18-9845-2018 (cit. on p. 27).

Pöschl, U. (2005). "Atmospheric Aerosols: Composition, Transformation, Climate and Health Effects". *Angew. Chem. Int. Ed.* 44.46, pp. 7520–7540. DOI: 10.1002/anie.200501122 (cit. on pp. 3, 9).

Purcell, E. M. and C. R. Pennypacker (1973). "Scattering and absorption of light by nonspherical dielectric grains". *Astrophys. J.* 186, pp. 705–714. DOI: 10.1086/152538 (cit. on p. 23).

Schnaiter, M., S. Büttner, O. Möhler, J. Skrotzki, M. Vragel, and R. Wagner (2012). "Influence of particle size and shape on the backscattering linear depolarisation ratio of small ice crystals - cloud chamber measurements in the context of contrail

and cirrus microphysics". *Atmos. Chem. Phys.* 12.21, pp. 10465–10484. DOI: 10.5194/acp-12-10465-2012 (cit. on p. 21).

Schnitzler, E. G., A. Dutt, A. M. Charbonneau, J. S. Olfert, and W. Jäger (2014). "Soot Aggregate Restructuring Due to Coatings of Secondary Organic Aerosol Derived from Aromatic Precursors". *Environ. Sci. Technol.* 48.24. PMID: 25390075, pp. 14309–14316. DOI: 10.1021/es503699b (cit. on p. 27).

Seinfeld, J. H. and S. N. Pandis (2016). *Atmospheric Chemistry and Physics : From Air Pollution to Climate Change*. New York, United States: John Wiley & Sons, Incorporated. ISBN: 9781119221166 (cit. on pp. 5, 9, 10).

Skorupski, K. and J. Mroczka (2014). "Effect of the necking phenomenon on the optical properties of soot particles". *J. Quant. Spectrosc. Radiat. Transfer* 141.Supplement C, pp. 40–48. ISSN: 0022-4073. DOI: 10.1016/j.jqsrt.2014.03.001 (cit. on p. 27).

Sorensen, C. M. (2001). "Light Scattering by Fractal Aggregates: A Review". *Aerosol Sci. Technol.* 35, pp. 648–687. DOI: 10.1080/02786820117868 (cit. on p. 26).

Stull, R. B. (1988). "Mean Boundary Layer Characteristics". In: *An Introduction to Boundary Layer Meteorology*. Ed. by R. B. Stull. Dordrecht: Springer Netherlands, pp. 1–27. ISBN: 978-94-009-3027-8. DOI: 10.1007/978-94-009-3027-8_1 (cit. on p. 7).

Takano, Y. and K. Jayaweera (1985). "Scattering phase matrix for hexagonal ice crystals computed from ray optics". *Appl. Opt.* 24.19, pp. 3254–3263. DOI: 10.1364/AO.24.003254 (cit. on p. 21).

Teng, S., C. Liu, M. Schnaiter, R. K. Chakrabarty, and F. Liu (2019). "Accounting for the effects of nonideal minor structures on the optical properties of black carbon aerosols". *Atmos. Chem. Phys.* 19.5, pp. 2917–2931. DOI: 10.5194/acp-19-2917-2019 (cit. on pp. 25, 27).

Tesche, M., A. Kolgotin, M. Haarig, S. P. Burton, R. A. Ferrare, C. A. Hostetler, and D. Müller (2019). "3+2+X: what is the most useful depolarization input for retrieving microphysical properties of non-spherical particles from lidar measurements using the spheroid model of Dubovik et al. (2006)?" *Atmos. Meas. Tech.* 12.8, pp. 4421–4437. DOI: 10.5194/amt-12-4421-2019 (cit. on p. 16).

U.S. Commitee on Extension of the Standard Atmosphere (1976). *U.S. Standard Atmosphere*. Tech. rep. U.S. Government Printing Office. URL: https://ntrs.nasa.gov/archive/nasa/casi.ntrs.nasa.gov/19770009539.pdf (cit. on p. 6).

Wandinger, U. (2005). "Introduction to Lidar". In: *Lidar: Range-Resolved Optical Remote Sensing of the Atmosphere*. Ed. by C. Weitkamp. New York, NY: Springer New York, pp. 1–18. ISBN: 978-0-387-25101-1. DOI: 10.1007/0-387-25101-4_1 (cit. on p. 16).

Waterman, P. C. (1965). "Matrix formulation of electromagnetic scattering". *Proc. IEEE* 53.8, pp. 805–812. ISSN: 0018-9219. DOI: 10.1109/PROC.1965.4058 (cit. on p. 23).

Wells, N. C. (2011). *The Atmosphere and Ocean: A Physical Introduction*. 3rd Edition. John Wiley & Sons, Inc. (cit. on pp. 5, 6).

Wiegner, M., J. Gasteiger, K. Kandler, B. Weinzierl, K. Rasp, M. Esselborn, V. Freudenthaler, B. Heese, C. Toledano, M. Tesche, and D. Althausen (2009). "Numerical simulations of optical properties of Saharan dust aerosols with emphasis on lidar applications". *Tellus B* 61.1, pp. 180–194. DOI: 10.1111/j.1600-0889.2008.00381.x (cit. on p. 28).

Wood, R. (2012). "Stratocumulus Clouds". *Mon. Weather Rev.* 140.8, pp. 2373–2423. DOI: 10.1175/MWR-D-11-00121.1 (cit. on p. 7).

Worringen, A., M. Ebert, T. Trautmann, S. Weinbruch, and G. Helas (2008). "Optical properties of internally mixed ammonium sulfate and soot particles–a study of individual aerosol particles and ambient aerosol populations". *Appl. Opt.* 47.21, pp. 3835–3845. DOI: 10.1364/AO.47.003835 (cit. on p. 27).

Wu, Y., T. Cheng, X. Gu, L. Zheng, H. Chen, and H. Xu (2014). "The single scattering properties of soot aggregates with concentric core–shell spherical monomers". *J. Quant. Spectrosc. Radiat. Transfer* 135.Supplement C, pp. 9–19. ISSN: 0022-4073. DOI: 10.1016/j.jqsrt.2013.11.009 (cit. on p. 28).

Wu, Y., T. Cheng, L. Zheng, and H. Chen (2016). "Models for the optical simulations of fractal aggregated soot particles thinly coated with non-absorbing aerosols". *J. Quant. Spectrosc. Radiat. Transfer* 182.Supplement C, pp. 1–11. DOI: 10.1016/j.jqsrt.2016.05.011 (cit. on p. 29).

Wu, Y., T. Cheng, L. Zheng, and H. Chen (2017). "Sensitivity of mixing states on optical properties of fresh secondary organic carbon aerosols". *J. Quant. Spectrosc. Radiat. Transfer* 195.Supplement C, pp. 147–155. DOI: 10.1016/j.jqsrt.2017.01.013 (cit. on pp. 25, 28).

Wu, Y., T. Cheng, L. Zheng, H. Chen, and H. Xu (2015). "Single scattering properties of semi-embedded soot morphologies with intersecting and non-intersecting surfaces of absorbing spheres and non-absorbing host". *J. Quant. Spectrosc. Radiat. Transfer* 157.Supplement C, pp. 1–13. ISSN: 0022-4073. DOI: 10.1016/j.jqsrt.2015.02.006 (cit. on p. 29).

Xiong, C. and S. K. Friedlander (2001). "Morphological properties of atmospheric aerosol aggregates". *Proc. Natl. Acad. Sci. U.S.A.* 98.21, pp. 11851–11856. ISSN: 0027-8424. DOI: 10.1073/pnas.211376098 (cit. on p. 26).

Yon, J., A. Bescond, and F. Liu (2015). "On the radiative properties of soot aggregates part 1: Necking and overlapping". *J. Quant. Spectrosc. Radiat. Transfer* 162.Supplement C. DOI: 10.1016/j.jqsrt.2015.03.027 (cit. on p. 27).

Yurkin, M. A. and A. G. Hoekstra (2007). "The discrete dipole approximation: An overview and recent developments". *J. Quant. Spectrosc. Radiat. Transfer* 106.1. IX Conference on Electromagnetic and Light Scattering by Non-Spherical Particles, pp. 558–589. DOI: 10.1016/j.jqsrt.2007.01.034 (cit. on p. 23).

Yurkin, M. A. and A. G. Hoekstra (2011). "The discrete-dipole-approximation code ADDA: Capabilities and known limitations". *J. Quant. Spectrosc. Radiat. Transfer* 112.13. DOI: 10.1016/j.jqsrt.2011.01.031 (cit. on p. 23).

Zdunkowski, W., T. Trautmann, and A. Bott (2007). *Radiation in the atmosphere: a course in theoretical meteorology*. Cambridge University Press. ISBN: 978-1-108-46272-3 (cit. on pp. 17–19, 21, 22).

Zhang, R., A. F. Khalizov, J. Pagels, D. Zhang, H. Xue, and P. H. McMurry (2008). "Variability in morphology, hygroscopicity, and optical properties of soot aerosols during atmospheric processing". *Proc. Natl. Acad. Sci. U.S.A.* 105.30, pp. 10291–10296. DOI: 10.1073/pnas.0804860105 (cit. on p. 27).